Acta Materialia 173 (2019) 61–73

Contents lists available at ScienceDirect

Acta Materialia

journal homepage: www.elsevier.com/locate/actamat

Full length article

3D printing of biomimetic composites with improved fracture toughness

Zian Jia, Lifeng Wang*

Department of Mechanical Engineering, State University of New York at Stony Brook, Stony Brook, NY, 11794, USA

ARTICLE INFO

Article history:
Received 28 November 2018
Received in revised form
1 April 2019
Accepted 24 April 2019
Available online 30 April 2019

Keywords:
Biomimetic composites
Toughness
Crack arresting
Architected materials
3D printing

ABSTRACT

Recent researches show that material microstructural designs mimicking biomaterials offer an effective way to produce tougher composites. To reveal the underlying microstructure-toughness relationship, five bioinspired material microstructures are investigated experimentally, including the brick-and-mortar, cross-lamellar, concentric hexagonal, and rotating plywood microstructures. The feature sizes of these microstructures are controlled to be one order smaller than the specimen size, providing better pictures of how crack resistance interacts with heterogeneity. Fracture theories are further used to analyze the toughening mechanisms and find the design criteria. Results show that the rotating plywood structure presents a "J" shaped *R*-curve, while other structures show "Γ" shaped *R*-curves. The "J" shaped *R*-curve gives a larger critical energy release rate and tolerates a longer crack, thus preferable for crack arresting. By contrast, the "Γ" shaped *R*-curve provides a larger critical failure stress and is beneficial for preventing crack initiation. Moreover, combined experimental results and theoretical analysis suggest that heterogeneity improves toughness by 1) creating stiffness variations to slow down crack propagation and prevent crack penetration and 2) guiding cracks along weak interfaces to promote progressive damage. Our results shed new light on the structure-property relationship that will facilitate the design of tougher and better crack resistant composites.

1. Introduction

High strength (a material's resistance to non-recoverable deformation) and high toughness (a material's resistance to fracture) are two basic requirements for almost all engineering materials. However, a strong material often lacks toughness [1,2]. For example, monolithic ceramics are strong but brittle, carbon fibers break at a high-stress level but at a small strain [3]. In recent decades, the toughness-strength tradeoff is largely tackled by developing architected composites with finely controlled microstructures, which introduce extrinsic toughening mechanisms [1,4,5]. For instance, mimicking the nacreous layer of abalone shells, ceramic plates are pressed and sintered into staggered configurations, achieving hundreds of times improved toughness [6,7]. Using carbon fibers as reinforcements of polymer matrices, stiff, strong, and tough composites can be obtained with a proper matrix property [8]. Moreover, distributing coarse grain layers and ultrafine grain layers alternatively at the micrometer scale produces stronger and tougher metals [9]. These studies demonstrate how microstructures can be designed to improve toughness. However, traditional fabrication methods like press and sintering [6], layer by layer deposition [10], and repeated rolling [9] cannot produce microstructures of arbitrary geometry [11].

Recent advances in 3D printing make the fabrication of 3D microstructures with arbitrary geometry possible and have promoted a surge in the study of biomimetic composites [12–16]. For example, staggered microstructures inspired from bones [15] were printed with a multi-material printer, realizing over 10 times increase in fracture energy under static tensile loading. Similar methods were used to study the role of osteon shape [17], interfacial waviness [18], and mineral bridges [19], uncovering the design motifs of biomaterials. Besides polymers based 3D printing, metals with dislocations arranged in hexagonal networks are printed with a selective laser melting method, improving strength and ductility simultaneously [20]. Furthermore, with the aid of magnetic fields and nozzle rotation, fiber

* Corresponding author.
E-mail address: lifeng.wang@stonybrook.edu (L. Wang).

https://doi.org/10.1016/j.actamat.2019.04.052
1359-6454/

directions are controlled to arrange in concentric [21], layered [22], and spiral patterns [14], offering tunable stiffness and >100% strength improvement [14]. More recently, multiple bio-inspired microstructures are integrated into one specimen using hierarchical/hybrid design approaches [2,23], giving rise to 6 times improvement in impact resistance as well as tailored dynamic performance combinations.

These works on printing biomimetic composites improve our understanding of how material architecture can be controlled to produce tougher engineering materials. But there are still many open questions. First, most researches focus on one specific material microstructure while systematic comparisons between different microstructures are highly desired. Analyzing the fracture behavior of different microstructures provides insights into why specific microstructures are selected by nature in specific organisms. Besides, a systematic comparison also benefits the rational selection of material microstructure in engineering applications. Second, when testing biomaterial specimens, the size of the material microstructure is many orders (typically >3) smaller than the crack length and the specimen size. In such a scenario, only the macroscopic performance of the biomaterial can be presented. A more detailed picture – the interaction between crack resistance and heterogeneity, is hard to be revealed. In contrast, studying 3D printed specimens with microstructural length scale about 1 order smaller than the specimen size brings a more detailed picture of the microstructure-crack resistance relationship [18,24,25]. Third, many fracture models that consider crack propagation in heterogeneous materials [26] and anisotropic materials [27,28] have been proposed. Problems including crack deflection at dissimilar material interfaces [29], crack branching when encountering hard inclusions [30], and crack twisting guided by spiral interface [31–33] have been solved. While many studies have extended these theoretical models with FEM simulations [34,35], the application of these theories to 3D printed materials and to guide the design of bio-inspired microstructures are rather limited.

In this work, we design architected specimens for compact tension (CT) fracture test. The brick-and-mortar, cross-lamellar, concentric hexagonal, and rotating plywood microstructures (Fig. 1) are fabricated with a multi-material 3D printer, mimicking the microstructures of nacre, conch shell, bone osteon, and stomatopod dactyl club, respectively. The feature sizes of these microstructures are controlled to be about one order smaller than the specimen size. Subsequently, the fracture toughness is evaluated using a nonlinear elastic *J*-integral approach. Fracture theories are further used to analyze the experimental results and find the toughening mechanisms. Finally, design criteria for these microstructures are proposed.

2. Materials and methods

2.1. Microstructure design and specimen fabrication

In this study, the biomimetic composites are restrained to be composed of a hard phase and a soft phase. The microstructures investigated here include the brick and mortar, concentric hexagon, cross-lamellar, branch-lamellar, and rotating plywood microstructures (Fig. 1). The brick and mortar structure is well known for its high toughness [15,36]. For simplicity, all bricks are assumed to have the same size and are arranged periodically. The concentric structures are found in bone osteons, blood vessels, and plant annual rings. To occupy the total plane, the concentric structure is modeled as concentric hexagons (Fig. 1b). The branch-lamellar structure is created mimicking the crack branching mechanism in conch shell [11] and the cross-lamellar model is adopted from Ref. [39] for comparison. Finally, the rotating plywood microstructure has been reported in stomatopod [40], teleost scales [41], and human teeth [42] for its outstanding fracture tolerance. Here, the model is constructed by stacking laminas with a constant angle of rotation (Fig. 1d). The geometries of all microstructures are summarized in Fig. 1. The soft phase volume fraction for each structure is (derivation provided in Supplementary Material),

$$V_{soft}^{B\&M} = 1 - \frac{\rho a^2}{(a+t)(\rho a + t)}, \tag{1}$$

$$V_{soft}^{Con.\ \ hex.} = \frac{2N^2 at + 2(N^2+N)t^2}{2(N^2+3N-1/2)a^2 + (4N^2+5N-1)at + 2(N^2+N)t^2}, \tag{2}$$

$$V_{soft}^{Branch-lamellar} = 1 - \frac{ab}{(a+t)(b+t)}, \tag{3}$$

$$V_{soft}^{Cross-lamellar} = 1 - \frac{abc}{(a+t)(b+t)(c+t)}, \tag{4}$$

$$V_{soft}^{Plywood} = \frac{t^2 + 2at}{(a+t)^2}, \tag{5}$$

where a, b, c, and t are the geometric parameters shown in Fig. 1, ρ is the aspect ratio of the brick in the brick and mortar microsturcutre, and N is the layer number of the concentric structure. Using these formulas, the geometric parameters of the microstructures are calculated such that V_{soft} of all microstructures are 0.25, except that of the concentric hexagonal structure is 0.50 (since bone has a greater volume fraction of soft phase [43]). All sizes used in manufacturing are listed in Table S1, Supplementary Material.

These microstructures are then 3D printed into 45 mm × 40 mm × 8 mm ($H \times L \times B$) CT specimens using a commercial Objet Connex260 3D printer (Stratasys corporation) (Fig. 2c). The printer is capable to print multiple materials simultaneously and has a print precision of 30 μm in the layer deposition direction and 600 DPI (43 μm) in the print plane. The printed crack front is further sharpened with a fresh razor blade ensuring that the notch curvature is much smaller than the corresponding plastic processing zone [44]. The two constituent materials are a glassy polymer verowhite (the hard phase) and a rubbery polymer tango plus (the soft phase). Their force-displacement curves under fracture test are plotted in Fig. 2a. Specifically, the hard phase has a Young's modulus $E_h = 1.56$ GPa, Poisson's ratio $\nu = 0.33$, and fracture toughness $G_{IC} = 0.95$ kJ/m^2, while the soft phase has a Young's modulus $E_s = 4$ MPa, Poisson's ratio $\nu = 0.4$, and fracture toughness $G_{IC} = 0.20$ kJ/m^2 [45]. The high modulus contrast ($E_h/E_s = 390$) is consistent with that of biomaterials, e.g., the hard mineral in nacre hasYoung's modulus of 100 GPa, while the interface has a shear modulus of 30–60 MPa [46,47].

2.2. Compact tension (CT) fracture test

The fracture toughness is determined using compact tension (CT) fracture tests referring to the ASTM standard E1820, where the J integral is calculated by adding the elastic part J_{el} and the plastic part J_{pl}, $J = J_{el} + J_{pl}$. Although this method is originally developed to

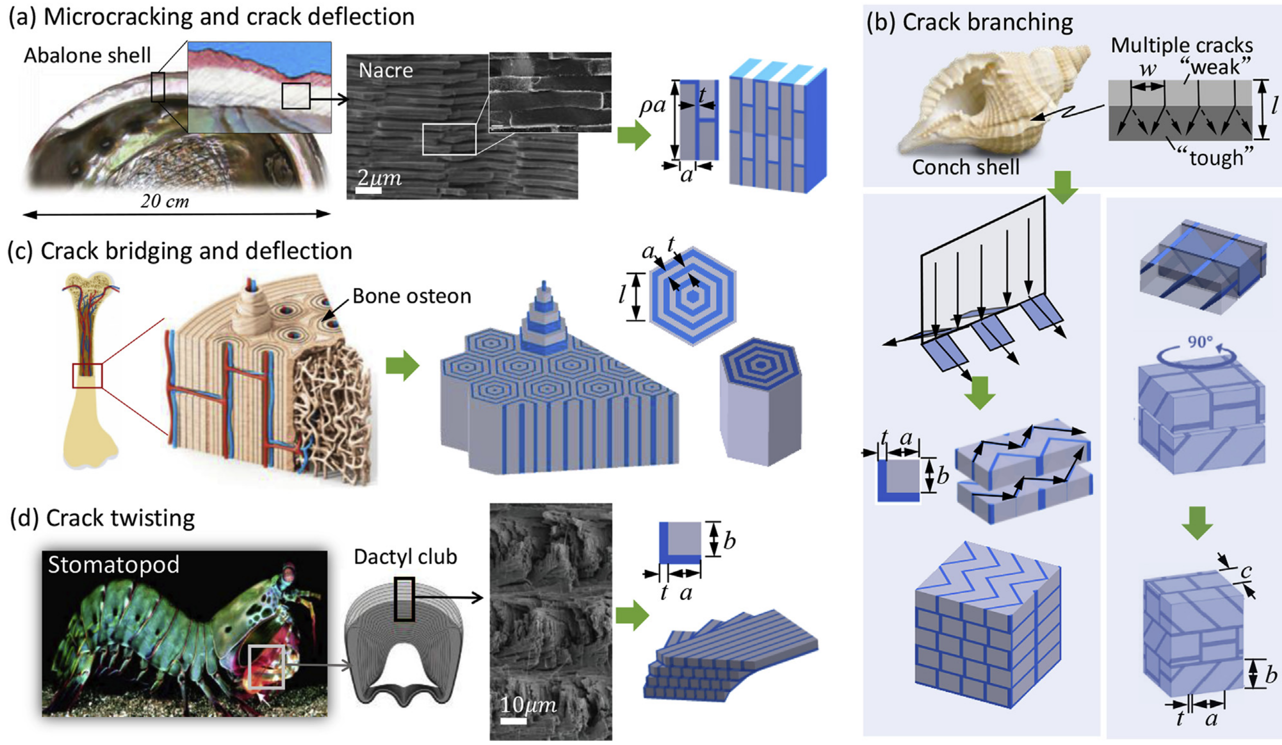

Fig. 1. The design of the biomimetic microstructures. (a) The brick and mortar microstructure in the nacreous layer of an abalone shell. (b) Top shows the crack branching mechanism observed in conch shells. Bottom shows the branch-lamellar (left) and cross-lamellar (right) microstructures mimicking the tough layer of the conch shell. (c) The concentric hexagonal microstructure mimicking the bone osteon structures. (d) The rotating plywood microstructure in the stomatopod dactyl club. The images in (a), (c), and (d) are adapted from Refs. [36–38], respectively. The grey and blue color in the schematics represent the hard phase and soft phase respectively. Also marked are the geometric parameters defining the unit cells. (For interpretation of the references to color in this figure legend, the reader is referred to the Web version of this article.)

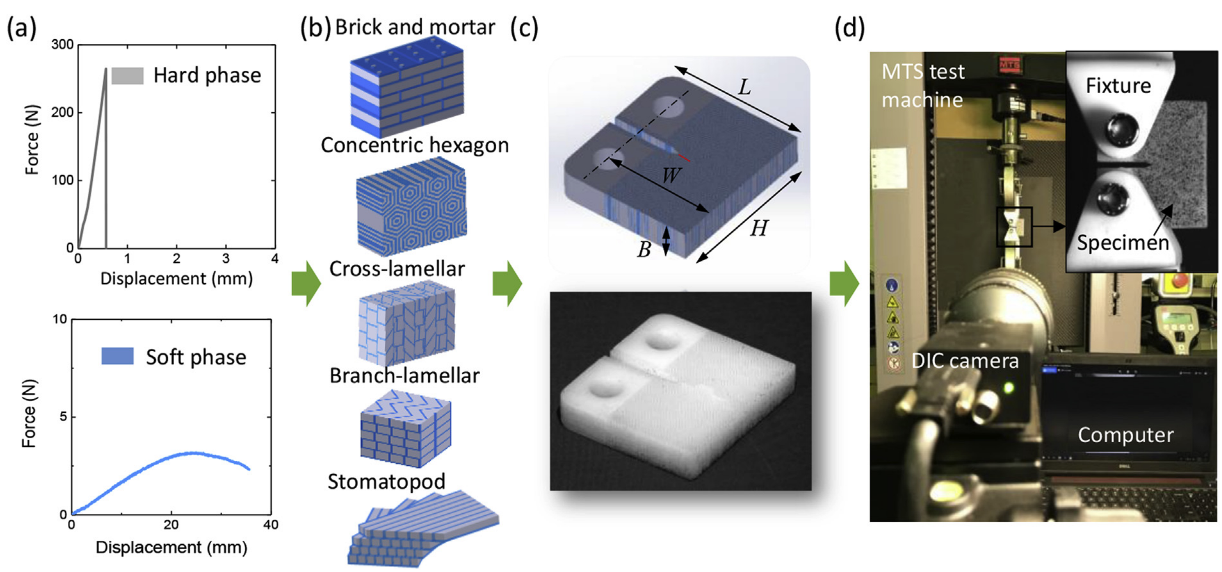

Fig. 2. (a) The force-displacement curves of the hard phase (top) and soft phase (bottom) from the fracture test. (b) shows the microstructural elements. (c) 3D model and the fabricated specimen. The red line highlights the crack tip sharpened by a razor blade. (d) Experiment set up of the fracture test. (For interpretation of the references to color in this figure legend, the reader is referred to the Web version of this article.)

determine the fracture toughness of homogeneous metallic materials, it has been adopted to evaluate the fracture toughness of heterogeneous materials in many studies [48–50]. The applicability of the ASTM standard here can be rationalized as follows: 1) the method is based on elastic-plastic fracture mechanics. The plastic part, J_{pl}, is calculated by an energy approach which is a function of the specimen size, crack length, and the increment of the plastic area under the load versus plastic load-line displacement. The method of calculating the plastic area increment is extended to heterogeneous materials. 2) The original equation for calculating the elastic part, J_{el}, is not exact for heterogeneous materials. In this study, formulas for orthotropic material are adopted to evaluate J_{el} [50,51].

Following the standard procedure, the elastic component is calculated from the stress intensity factor $K_{(i)}$, as $J_{el} = K_{(i)}(1-\nu^2)/E'$, where ν is Poisson's Ratio, E' is the effective Young's modulus based on an orthotropic material assumption [51], and the subscript i denotes values at crack length a_i. $K_{(i)}$ is given by

$$K_{(i)} = \frac{P_i}{B\sqrt{W}} f(a_i/W), \tag{6}$$

where P_i is the instantaneous load, the definition of B and W are specimen depth and width depicted in Fig. 2c. $f(a_i/W)$ is a polynomial of a_i/W provided in the Supplementary Material. The plastic part is calculated with an incremental approach

$$J_{pl(i)} = \left[J_{pl(i-1)} + \left(\frac{\eta_{(i-1)}}{b_{(i-1)}}\right) \frac{A_{pl(i)} - A_{pl(i-1)}}{B_N}\right] \cdot \left[1 - \gamma_{(i-1)} \frac{a_{(i)} - a_{(i-1)}}{b_{(i-1)}}\right], \tag{7}$$

where $\eta_{(i-1)} = 2.0 + 0.522 b_{(i-1)}/W$, $\gamma_{(i-1)} = 1.0 + 0.76 b_{(i-1)}/W$, $b_{(i)} = W - a_i$, and $A_{pl(i)} - A_{pl(i-1)}$ is the increment of plastic work as crack propagates from a_{i-1} to a_i. The fracture tests are performed at a constant displacement rate of 1.0 mm/min. During the test, videos are recorded and used to calculate the strain fields with a digital image correlation (DIC) method (VIC-2D, Correlated Solution Inc.). More details are provided in the Supplementary Material.

3. Results

3.1. The brick and mortar structure

To obtain tough brick and mortar biomimetic composites, the geometry [37], interfacial mineral bridge [52], and surface asperity [53] should be rationally designed. Previously, finite element method (FEM) [54] and hybrid sputtering [55] have been used to study the effect of micro-asperity [55]. Here, we propose a simple method to create interfaces with two levels of micro-asperity by controlling the print direction (Fig. 3a). Our printer uses a PolyJet technique, where photopolymer liquids are dropped onto a build tray layer by layer and followed by UV light cure. Each liquid drop is in an elliptical shape with the longitudinal direction oriented toward the print direction as depicted in Fig. 3a and Fig. S15. Thereby, a print direction parallel to the interface produces a low asperity interface and a print direction perpendicular to the interface gives a high asperity interface. By contrast, the cylindrical hard bridges can be modeled and printed more straightforwardly (Fig. 3b) [19]. The number and the radius of bridges are controlled such that the total volume fraction of the soft phase is kept at 0.25 (Supplementary Material).

To realize the optimal strength design, a balance between the tensile stress of the brick and the shear stress of the mortar is required [56,57]. In a shear lag model considering stress concentration [46], the optimal strength criteria entails the yield stress of the interface (S_{int}) to be at the same level of the tensile strength of the hard bricks (S_{BR}) divided by the aspect ratio, $S_{int} = S_{BR}/C\rho$, where C is the stress concentration factor which depends on E_h/E_s and ρ. Recognizing that introducing mineral bridges and asperities are mechanisms that improve the interfacial shear strength, therefore, the new optimal stress balance condition can be written as,

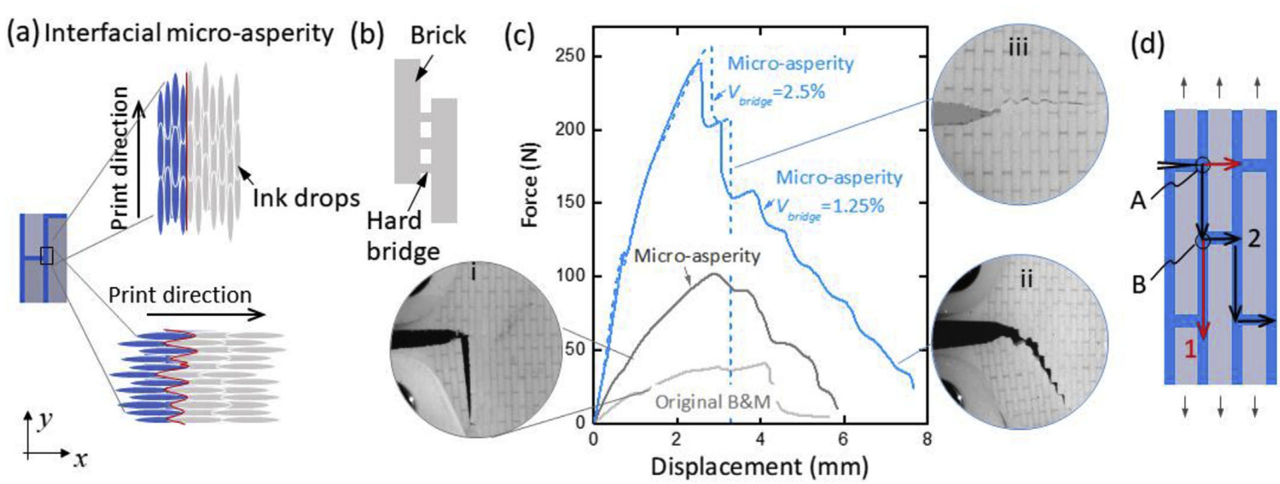

Fig. 3. The brick and mortar structure. (a) Print direction is used to control the interfacial micro-asperity. (b) Bridges are introduced between adjacent bricks. (c) The force-displacement curves of the original brick and mortar microstructure and designs with micro-asperity and hard bridges. (i-iii) show the corresponding crack patterns. (d) The preferred stair-like crack path (black arrow) is formed when crack deflection takes place at both point A and point B. The red arrows show crack paths to be avoided. (For interpretation of the references to color in this figure legend, the reader is referred to the Web version of this article.)

$$\eta S_{int} + \frac{V_{bridge}}{V_{soft}} S_{bridge} = \frac{S_{BR}}{C\rho}, \tag{8}$$

where η is the magnification factor introduced by interfacial asperity and S_{bridge} is the shear strength of the hard bridge. Optimal designs require the left hand side (LHS) of Eq. (8) to be slightly smaller than the right hand side (RHS), such that matrix yielding takes place before the breakage of bricks. Note that this condition only ensures that shear failure takes place before the break of the brick, but it does not predict the crack path. To form a progressive stair-like crack pattern [Fig. 3c(ii)], additional conditions on crack deflection should be considered. Conversely, when the right side is greater, the crack will penetrate the brick and the specimen fails catastrophically [58,59]. In our experiment, these values are estimated as $S_{bridge} = S_{BR} = 46.6$ MPa, $S_{int} = 1.0$ MPa, $\eta \approx 2$ (the high asperity surface), and $C \approx 2.1$ [46]. Based on these data, we design four types of brick and mortar specimens (Table S2). The original design has no bridges and possesses a low asperity level. The micro-asperity design has a higher asperity but no bridges. The third design has $V_{bridge} = 1.25\%$ and a high asperity interface (LHS slightly smaller than RHS), while the fourth design has $V_{bridge} = 2.5\%$ and a high asperity interface (LHS > RHS).

The resultant force-displacement curves are presented in Fig. 3c. As expected, only the design with $V_{bridge} = 2.5\%$ breaks catastrophically. Moreover, it is observed that higher micro-asperity brings better stiffness, strength, and work of fracture. The reason is that higher asperity increases contact and slide at the interface, thus more energy is required to propagate the crack [60].

Although a higher micro-asperity enhances the performance quite significantly, however, the observed straight-through shear failure [Fig. 3c(i)] is still unfavorable. In which case, the crack propagates all the way through the weak interface with no crack deflection. To avoid the straight-through shear failure, crack must deflect at both locations A and B marked in Fig. 3d. The competition between crack deflection and penetration has been derived by He in Ref. [24]. The ratio of the energy release rate of crack deflection (G^d) to crack penetration (G^p) can be estimated by (Supplementary Material),

$$G^d \Big/ G^p = 0.254 \Big/ \left(1 - \alpha^{1.2}\right), \tag{9}$$

where $\alpha = (\overline{E}_2 - \overline{E}_1)/(\overline{E}_1 + \overline{E}_2)$, with $\overline{E}_i = E_i/(1-\nu^2)$ for plane strain. E_2 and E_1 are Young's modulus of the material in front and behind the crack tip, respectively. A stair-like path is formed when the crack deflects at point A and point B, which requires,

$$\frac{R_{m1}}{R_b} < \left.\frac{G^d}{G^p}\right|_{E_2 \gg E_1} \to \infty, \tag{10}$$

at point A and

$$\frac{R_{m2}}{R_{m1}} < \left.\frac{G^d}{G^p}\right|_{E_2 = E_1} = 0.254, \tag{11}$$

at point B where R_b is the crack resistance of the brick, R_{m1} and R_{m2} represent the crack resistance of the matrix along the vertical direction and horizontal direction, respectively (Fig. 3d). Eq. (10) shows that a high modulus contrast (in our experiment $E_h/E_s = 390$) promotes crack deflection at location A. Eq. (11) shows that the vertical matrix should be tougher than the horizontal matrix ($R_{m1} > R_{m2}$) to avoid straight-through shear failure. This explains why the plates in nacres present waviness, asperity, and mineral bridges on their side surfaces [36,52]. Similarly, introducing asperity and 1.25% hard bridges ensures $R_{m1} > R_{m2}$ and prevents straight-through shear failure. The resultant stair-like crack path is depicted in Fig. 3c(ii), which shows improved stiffness, strength, and toughness. The fracture energy is 15 times that of the hard phase and 7 times that of the original brick and mortar design, indicating the importance of micro-asperity and mineral bridges in toughening brick and mortar structures.

To further understand the toughening mechanism, strain fields are visualized by DIC. Fig. 4a presents that while the homogeneous specimen only shows localized stains at the crack tip, the brick and mortar specimens show strains localized in multiple sites thus forming a larger fracture processing zone. Moreover, the original brick and mortar specimen shows large shear strains but negligible tensile strains. Adding interfacial asperity and bridges reduces the shear strain and increases the tensile strain. Importantly, the stair-like crack pattern [Fig. 4a(iv)] exhibits a comparable level of shear strain and tensile strain, validating that a balance between tensile deformation and shear deformation is critical for designing tough brick and mortar structures. The work of fracture and maximum stress at failure are further shown in Fig. 4b, revealing that up to 60% of the fracture energy arises from the progressive crack propagation stage.

3.2. The lamellar structure

The toughness of conch shells is reported to be 2–3 orders higher than its hard constituent. The mechanism of such high toughness has been revealed as multiple crack initiation at a weak layer followed by crack bridging in a tough layer (Fig. 1b) [61,62]. Qualitatively, a higher crack density can be obtained by a larger toughness contrast between the weak and tough layers [61]. In conch shell, the tough layer is constructed by cross-laying laminas. Mimicking this crack branching concept, two lamellar geometries are proposed (Fig. 5a and b), namely, the branch-lamellar structure and cross-lamellar structure [63]. Also plotted in Fig. 5a and b are the post-mortem fracture surfaces, showing that the cracks are confined to the weak layers forming 3D fracture surfaces. Crack bridging and pull out are found in the experiment without breakage the of hard materials, which leads to relatively smooth bell-shaped load-displacement curves (Fig. 5c).

Fig. 5d shows that the progressive crack propagation leads to rising crack resistance curves (R-curve). Specifically, the branch-lamellar structure exhibits a steady state crack resistance ~6 times that of crack initiation. As increasing energy is required for crack propagation, cracks tend to form elsewhere [64]. Thereby, when such a tough layer is combined with a weak layer depicted in Fig. 1b, multiple crack initiation can be formed. Another critical condition of forming multiple cracks is that coalesce of adjacent cracks should be avoided, this condition is visualized in Fig. 5e where deformations are limited to soft interface in front of the crack tip, preventing crack coalesce. Thereby, the rising R-curve and confined crack path are the two direct reasons for forming multiple cracks and thus critical to the high toughness of conch shells.

Let's next use the branch-lamellar microstructure as an example to quantitatively estimate the toughness improvement. Experiments suggest that crack deflection and crack bridging are two fundamental mechanisms of toughening. Crack deflection improves toughness by increasing the crack surface area and

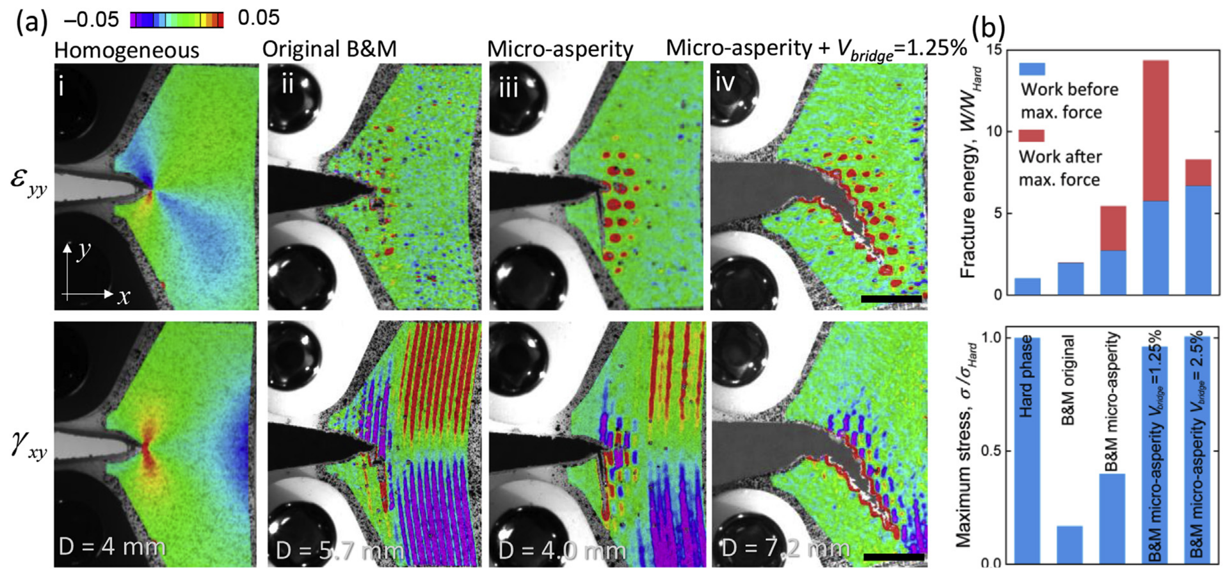

Fig. 4. (a) The strain field of the brick and mortar designs compared to that of a homogeneous specimen. The corresponding displacements are marked at the bottom of the snapshots. (b) Summary of the corresponding toughness (measured by the area under the force-displacement curve) and strength.

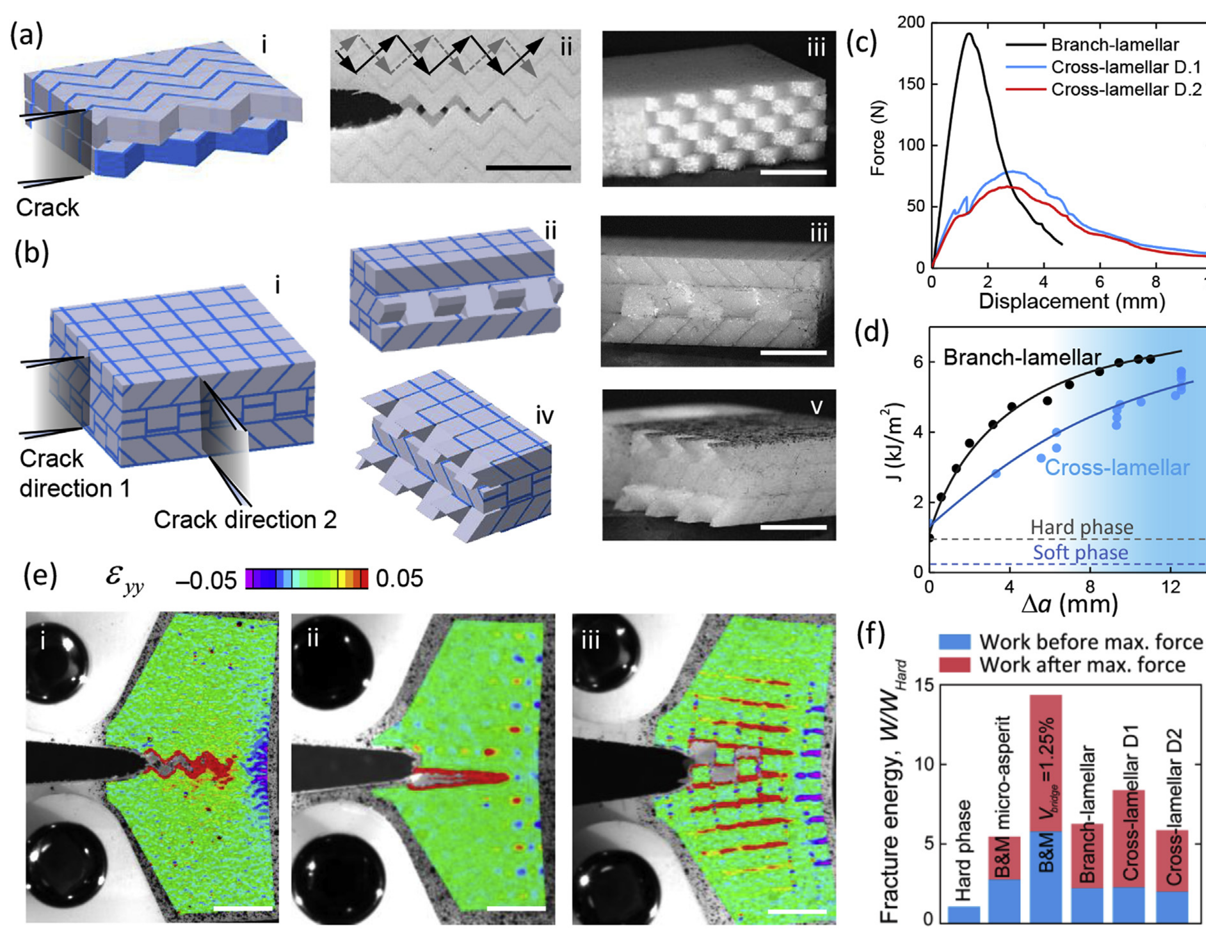

Fig. 5. (a) Cracking path of the branch-lamellar microstructure, (i) 3D model, (ii) in-situ picture, and (iii) post-mortem crack surface. (b) The cross-lamellar microstructure. (ii, iv) 3D model and (iii, v) post-mortem pictures. (c) The force-displacement curves. (d) The *R*-curves. The shaded area indicates the size-dependent region suggested by the ASTM standard. (e) Strain fields of (i) branch-lamellar, cross-lamellar with (ii) crack direction 1 and (iii) crack direction 2. (f) Fracture energy comparison between different material architectures. All scale bars represent 5 mm.

Table 1
Toughening mechanism in the branch-lamellar structure.

Mechanisms	Schematics	Formula	Evaluation
Crack resistance improved by mixed mode cracking		$R/R_1 = [1+(\lambda-1)\sin^2\psi]^{-1}$	1.114 (crack deflection) 3.333 (crack bridging)
Crack driving force reduced by crack deflection	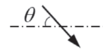	$G(\theta)/G_1 = \cos^2(\theta/2)(1+\cos\theta)/2$	0.729
Crack area improved by crack deflection		$S_d/S_1 = 1/\cos\theta$	1.414
Crack area introduced by crack bridging		$S_b/S_1 = (a+t)/(b+t)$	0.875

Note: R/R_1 is the mixed mode toughness normalized by pure mode I toughness. S_d/S_1 and S_b/S_1 represent the enlarged crack surface area by crack deflection and crack bridging compared to that of a flat interface. In the estimation, $\lambda = 0.3$, $\psi = 22.5°$ (deflection, estimated with $\theta = 45°$) and $= 90°$ (bridging), $\theta = 45°$, $a = 1.2$ mm, $b = 1.4$ mm, and $t = 0.2$ mm, see Supporting Information for detail.

introducing crack mode mixity. The surface area of the deflected crack is $1/\cos\theta$ times that of a straight crack, with θ being the tilt angle. Mode mixity improves the crack resistance of the interface, and at the same time, reduces the crack driving force. The crack resistance of an interface under mixed mode loading (R) compared to mode I loading (R_1) is [29],

$$R/R_1 = \left[1+(\lambda-1)\sin^2\psi\right]^{-1}, \tag{12}$$

where $\psi = \tan^{-1}(K_{II}/K_I)$ and λ is a parameter that controls the mode II contribution ($\lambda = 1$ for ideally brittle material). By contrast, the reduction in crack driving force is ([65], Supporting Information),

$$G(\theta)/G_1 = \cos^2(\theta/2)(1+\cos\theta)\Big/2. \tag{13}$$

The total toughness improvement by crack deflection can then be estimated as, $\frac{R}{R_1}\cdot\frac{G_1}{G}\cdot\frac{S_d}{S_1}$. The evaluation of each term is presented in Table 1, substitute the corresponding values into the above relation gives 2.16. A similar process can be adopted to evaluate the toughness improved by crack bridging, which gives $3.333 \times 0.875 = 2.91$ (Table 1). These values indicate that bridging has a slightly more important effect on toughness than crack deflection. Moreover, the total toughness is estimated to be 5.1 times that of a flat interface. Our experiment gives $J_{lam} = 6.08$ kJ/m^2 (the saturated value of J integral for the branch lamellar structure) and $J_{int} = 1.13$ kJ/m^2 (the J integral for a flat interface under mode I loading). Thus, the experimentally measured improvement, $J_{lam}/J_{int} = 5.38$, is consistent with the theoretical estimation.

Note that although the toughness improvements in the 3D printed specimens are quite significant (6 times of the hard phase), it is much smaller than that in the conch shells (2–3 orders). One reason is that multiple cracking does not take place in the CT specimen. If a specimen without precrack is loaded under tension or pure bending, multiple crack initiation and more significant toughness improvement may be envisioned.

3.3. *The concentric hexagonal structure*

When a crack propagates through the concentric hexagonal microstructure, it either deflects around the outermost hexagons or penetrates into the center. The first case is preferred in nature since important vascular or nutrition supply systems are often located in the center of a concentric structure. Based on fracture energy analysis, we can find the criteria of whether a crack will penetrate into the center of the hexagon. Suppose G_h and G_s are the fracture energy of the hard phase and soft phase, respectively. The energy of fracture required to penetrate n concentric layers of a unit cell can be derived as (Supplementary Materials)

$$W(n) = (2n-1)ahG_h + 3\left[l - \frac{2n-1}{2}a - \frac{2n-1}{6}t\right]hG_s, \tag{14}$$

where t, a, and l are geometric sizes defining the unit cell (Fig. 1), h is the out of plane height. Crack penetrating more concentric layers is not preferred if $\partial W(n)/\partial n > 0$, i.e., $W(n+1) - W(n) > 0$, which derives

$$2aG_h - (3a+t)G_s > 0. \tag{15}$$

Eq. (15) gives the condition to avoid crack penetration into the center, i.e., $G_h/G_s > (3a+t)/2a$. For a thin soft interface, $t \to 0$, the condition gives $G_h/G_s > 1.5$. For thick soft layer, e.g., $t = a$, it gives $G_h/G_s > 2$. In our experiments, the constituent properties correspond to $G_h/G_s = 5.1$. Therefore, cracks are predicted to deflect around the outermost hexagonal rings, which is consistent with the experimental results (Fig. 6a and b). Note that the outermost hexagonal structure is made of the hard phase, so cracks must penetrate at least one hard layer.

Having shown the condition of the preferred fracture pattern, we next analyze the toughening mechanism. The force-displacement curve, R-curve, and corresponding strain fields are presented in Fig. 6c–e. Interestingly, both the force-displacement curve and the R-curve show a stepped shape. The stepped force-displacement curve corresponds to the periodic break of the hard phase (marked by white arrows, Fig. 6a) and propagation of cracks along the weak phase (red arrow). When the crack penetrates a hard layer, the load drops instantaneously, the released strain energy is partially dissipated by the breakage of the hard phase. The remainder generates kinetic energy which drives a rapid crack propagation process [66]. This dynamic crack is slowed down by crack propagation along the soft interface (red arrow, Fig. 6a), which is eventually stopped when encountering the next hard layer (white arrows, Fig. 6a). To break the next hard layer, extra energy is required, thus crack resistance rises steeply (orange arrows, Fig. 6c and d). The evolution of the strain field during this process is plotted in Fig. 6e for reference. In summary, the concentric hexagonal microstructure is toughened by periodic cycles of 1) after breaking a hard layer, the released energy drives a dynamic crack propagation, 2) crack deflects along the interface reducing the crack propagation speed, 3) crack is stopped at the next hard layer, and 4) increasing load to break the hard layer, which starts the next cycle. This process repeats itself forming a stepped R-curve. Specifically, each cycle corresponds to a local “J” shape in the R-curve as

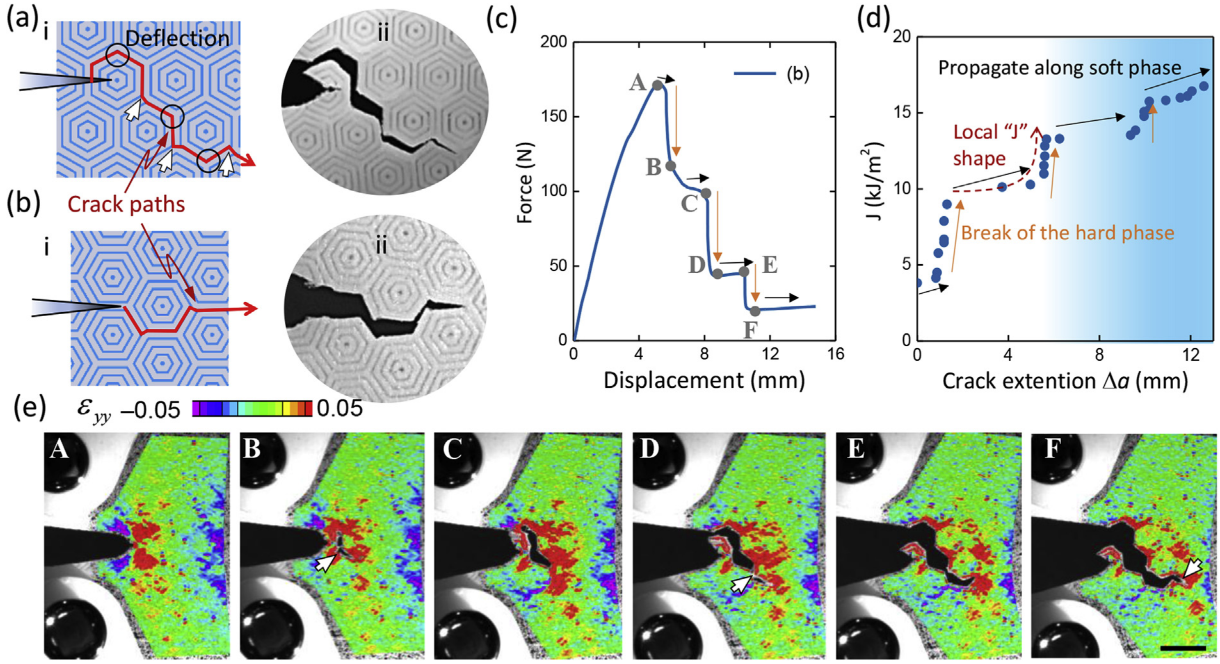

Fig. 6. Fracture performance of the concentric hexagonal microstructure. (a) and (b) show the crack propagation paths with two different crack incident directions. The black circles highlight crack deflection and the white arrows show locations of crack penetrating the hard phase. (c) Force vs displacement curve, (d) *R*-curve, and (e) normal strain fields correspond to (a). The strain contours A-F corresponds to the points in (c). Scale bar: 5 mm.

highlighted by red dashed arrow in Fig. 6d. Noted that the local "J" shape turns out to be quite common in heterogeneous materials as we'll discuss in section 4.3.

3.4. The rotating plywood structure

Compared to the brick and mortar microstructure of sea shells, it is reasonable to expect better toughness from their predator — the stomatopod [40]. Previous studies have shown that the high damage tolerance and crack arrest ability of stomatopod dactyl club are related to the rotating plywood microstructure [40,67]. To uncover the toughening mechanism of the rotating plywood microstructure, its *R*-curve is measured experimentally here. Fig. 7a depicts the direction of the incident crack with respect to the microstructure. The post-mortem specimen and strain field (Fig. 7) show that the crack is constrained to the soft phase and twists in a helicoidal manner. Fig. 7c schematically depicts the experimental observation that the crack surface projection (in the *xy* plane) expands approximately in a circular shape. Based on such a crack evolution process, the fracture energy required to propagate a crack by an extension of *da* can be derived as (Supplementary Material),

$$dW = (h - \pi a_0/2 + \pi a/2) \cdot da \cdot 2\gamma_{int}. \quad (16)$$

where γ_{int} is the crack surface energy, h is the specimen thickness, a_0 and a are the original crack length and total crack length, respectively. Fracture toughness (J integral) is then calculated as the fracture energy per unit fracture surface area $J = dW/hda$, giving

$$J = \left(2 - \frac{\pi a_0}{h}\right)\gamma_{int} + \frac{\pi \gamma_{int}}{h} a. \quad (17)$$

Eq. (17) suggest that when a crack expands steadily in a circular manner, J is proportional to the crack extension with a slope of $\pi\gamma^m_{int}/h$. Here, the superscript "*m*" is used to highlight the effect of mode mixity. Moreover, the force-displacement curve (Fig. 7d) is featured with an initial force drop followed by a steady force plateau. This result suggests that the fracture process can be characterized phenomenologically as a crack initiation stage and a steady crack extension stage [68]. In the initiation stage, the energy required for crack initiation equals $2\gamma^i_{int}$, where γ^i_{int} is the crack surface energy (with negligible mode mixity) (Fig. 7e). In the crack extension stage, the slope is calculated by linear fit giving a slope of 2.23×10^3 kJ/m^3 (Fig. 7e), which further derives $\gamma^m_{int} = 5.72$ kJ/m^2. The shape of the *R*-curve is therefore confined by a horizontal line at $J = 2\gamma^i_{int}$ and a tilted line with a slope of $\pi\gamma^m_{int}/h$. As such, γ^i_{int} and γ^m_{int} controls the shape of the *R*-curve. In our experiments, $\gamma^m_{int}/\gamma^i_{int} = 3.67$, which demonstrates the effect of mode mixity in toughening the twisted interface.

A twisting crack growing in the helicoidal architecture certainly amplifies crack surface per unit volume, therefore improving energy dissipation and stress relaxation in the dactyl club without leading to catastrophic failure.

4. Discussion

4.1. Comparison between different microstructures

Fig. 8a compares the representative force-displacement curves of different microstructures. The maximum force and work of fracture per mass are listed in Table 2. Results show that the brick and mortar structure exhibits the maximum load of failure (larger than the hard phase). Its work of fracture per mass is 14 times greater than the hard phase, making it both strong and tough. Moreover, the rotating plywood structure exhibits the maximum work of fracture per mass (17 times improvement),

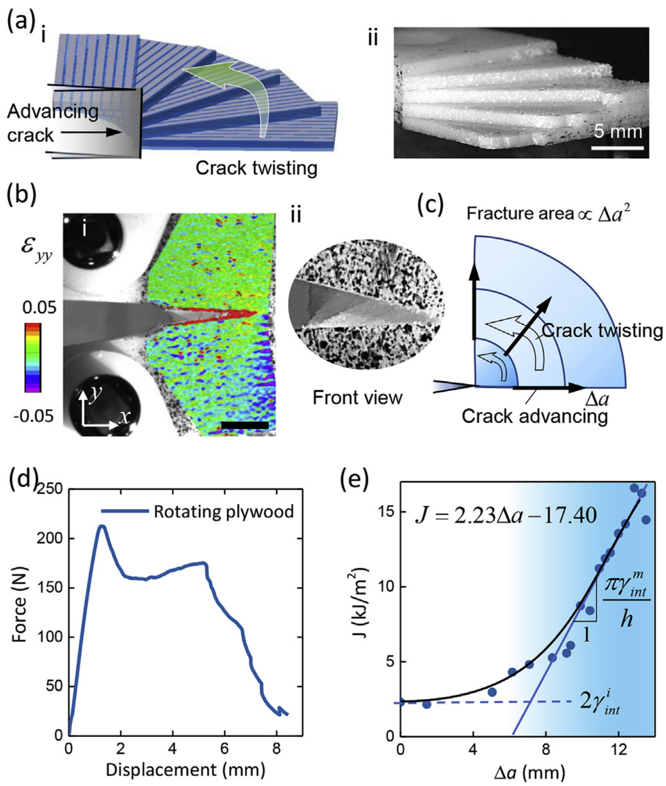

Fig. 7. The rotating plywood microstructure. (a) 3D model depicting the twisted crack surface in comparison with the experimental result. (b) shows the surface strain field obtained by DIC and the magnified crack front. (c) Schematic illustration of the crack surface, which expands in a quarter-circular manner. (d) and (e) show the force-displacement curve and crack resistance curve, respectively. Scale bar: 5 mm.

largely contributed by crack twisting. The concentric hexagonal structure exhibits a stair-like force-displacement curve and shows work of fracture improved by 15 times. Note that the crack propagation in the concentric hexagonal structure is intrinsically dynamic, but the concept of work of fracture is applicable because the kinetic energy released after breaking the hard phase is dissipated in the crack propagation process and at the end of the test, the kinetic energy of the specimen is negligible. Compared to the above structures, the lamellar structures show relatively small toughness improvements (5–8 times). Because in the lamellar structures, the cracks are confined to the interface, corresponding to a relatively small fracture processing zone. For realistic applications, the lamellar structures should be integrated with weak layers to form multiple cracks like in the conch shells [61].

Fig. 8b summarizes the *R*-curves of different structures, all showing a rising trend. Specifically, the rotating plywood structure exhibits a "J" shaped *R*-curve, while other structures present a "Γ" shaped *R*-curve. The "Γ" shape is common for most materials (e.g., metals, polymers, and tough ceramics), in which case the fracture process zone gradually increases and eventually saturates. The rotating plywood structure, by contrast, is characterized by a crack initiation stage and a crack extension stage. In the extension stage, the fracture area increases proportionally to Δa^2. Thereby, the crack resistance $\propto \Delta a$, forming the "J" shaped *R*-curve (section 3.4).

4.2. Shape of the R-curve

The shape of *R*-curves has significant influences on the stability of crack propagation. To illustrate this, Fig. 9 presents three types of *R*-curves, namely, the flat, "Γ" shaped, and "J" shaped. For single edged panel subjected to remote tensile stress σ, the crack driving force, G is proportional to crack length a [69]. This is represented by straight orange lines in Fig. 9. Unstable crack growth takes place when [66].

$$\frac{dG}{da} > \frac{dR}{da}. \tag{18}$$

For the flat *R*-curve shown in Fig. 9a, the critical load and critical energy release rate can be found graphically as σ_c and G_c. Crack becomes unstable when $\sigma > \sigma_c$. Because no crack propagation takes place before failure, the damage is catastrophic. By contrast, for the "Γ" shaped *R*-curve, crack will propagate from a_0 to a_c until instability occurs (Fig. 9b). Because cracks are stable when $a < a_c$, they are described as "arrested" cracks. For the "J" shaped *R*-curve, it is interesting that the crack growth will be arrested until reaching the end of the crack resistance curve. Note that there is a small unstable crack propagate region (marked by red in Fig. 9c), which will be arrested by the "J" shaped rising *R*-curve. This unstable crack propagation region, however, makes "J" shaped *R*-curves unfavorable for preventing crack initiation. Assume the "Γ" shaped and "J" shaped *R*-curves have the same end crack resistance (as in Fig. 9), the "J" shaped *R*-curve can achieve a larger critical energy release rate G_c and a

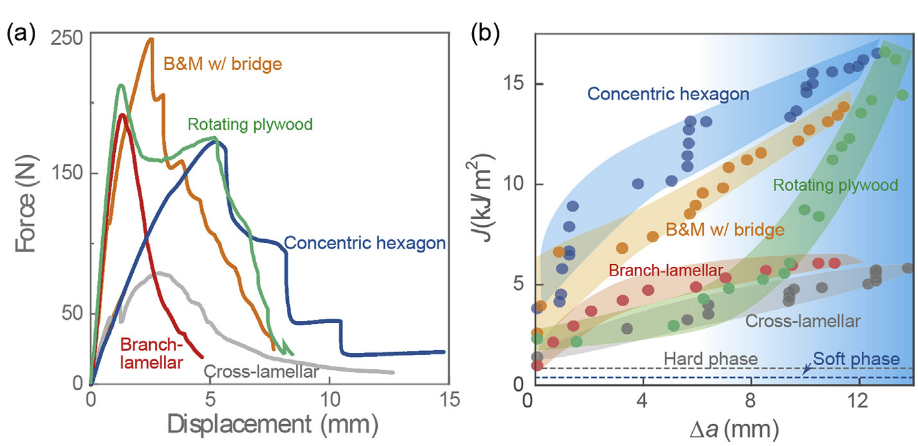

Fig. 8. A comparison between different bioinspired microstructures. (a) force-displacement curves and (b) crack resistance curves.

Table 2
Performance comparison between different microstructures.

Microstructure	Hard phase	Soft phase	Brick & mortar	Cross lamellar	Branch-lamellar	Concentric hexagon	Rotating plywood
Maximum force per mass, N/g	16.39	0.22	16.78	7.31	13.08	11.54	14.53
Total work per mass, N·mm/g	4.25	3.29	65.01	37.96	28.36	68.41	75.37
Total work per mass improvement	0.00	−0.23	14.28	7.93	5.67	15.08	16.72

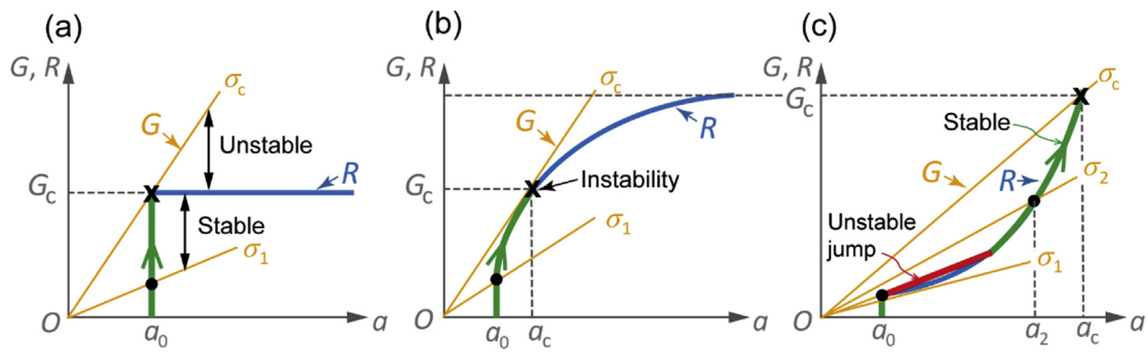

Fig. 9. Crack driving force versus *R*-curve diagrams for (a) flat *R*-curve, (b) "Γ" shaped *R*-curve, and (c) "J" shaped *R*-curve. *R* and *G* denote the crack resistance curve and the crack driving force respectively. The green color represents the "useful" range of the crack resistance curve under force-controlled load and the red color indicate the unstable jump. The subscript "c" notes critical values that lead to failure. (For interpretation of the references to color in this figure legend, the reader is referred to the Web version of this article.)

longer critical crack length a_c. Larger G_c and a_c means better crack arresting ability, which explains why the rotating plywood microstructure are found in biomaterials like teeth [42,70], teleost scales [41], and stomatopod dactyl club [40]. It should be noted that in a displacement controlled loading process, both the rising R-curves are stable. However, an impact event is dominantly load controlled [50], in which case the "useful" range of the "J" shaped *R*-curve is much larger than the "Γ" shaped *R*-curve. This might be a potential mechanism that contributes to stomatopod dactyl club in breaking sea shells. Moreover, while the "J" shaped *R*-curve exhibits a larger a_c, the "Γ" shaped *R*-curve is better at preventing crack initiation and exhibits a larger σ_c. This is beneficial to forming multiple cracks in a bilayer configuration (Fig. 1b), as in the conch shells [61].

4.3. Heterogeneity makes materials tougher

Results so far show that the material microstructure (heterogeneity) plays an important role in toughening composites. To obtain deeper insights of how heterogeneity works, let's consider a general situation: a crack is about to propagate through a bi-material composite with arbitrary microstructures (Fig. 10a). The crack either penetrates the material in front of it or propagates along paths confined by the weak phase. Based on this argument, we classify the effect of heterogeneity into two categories: 1) effect of material property variation when crack penetration takes place and 2) effect of forming complex fracture surfaces guided by weak interfaces.

The effect of material property change in front of a crack tip can be illustrated by the inhomogeneous model proposed in Ref. [71]. Consider a crack is propagating from material 1 with modulus E_1 toward material 2 with modulus E_2 (Fig. 10). The evolution of the energy release rate as the crack tip approaches to the interface can be solved by the configurational force method [71], which is reproduced in Fig. 10b–d (calculations summarized in Supplementary Material for completeness). J_{tip}/J_{far} represents the energy release rate at the crack tip compared to that of the remote field. Fig. 10b shows that when a crack propagates from a soft material toward a hard material, the driving force at the crack tip is reduced significantly ($J_{tip}/J_{far}<1$). Thus, crack propagation tends to be stopped. On the contrary, when cracks propagate from the hard phases to the soft phases, the driving force increases, thus crack penetration is facilitated. Periodic property changes is a special situation often encountered in heterogeneous materials, which leads to oscillating J_{tip}/J_{far} as depicted in Fig. 10d [25,31]. Note that for alternating property changes, $J_{tip}/J_{far}< 1$ still holds when the crack is propagating in the soft phase. These results conclude that a soft to stiff material property change plays an essential role in toughening the heterogeneous materials.

Moreover, these results on bi-material composites have implications on the design of gradient materials. For example, as an analogy to the bi-material system, when stiffness gradually decreases from the outer surface toward the inner region, cracks tend to propagate deep into the materials (Fig. 10c) [71]. Since gradient materials with stiffer outer layer are often adopted for better abrasion resistance, its deficiency in crack penetration protection should be highlighted. One solution to solve this problem is introducing a soft interface (Fig. 10d). Such a strategy is quite common in biomaterials, examples include the dentine-enamel junction in teeth and the cement lines in cortical bone.

On the other hand, when cracks are guided along the weak interfaces, the cracks often present tortuous paths and mixed mode loading (Fig. 10e). Specifically, the material is toughened by increasing the surface area of the crack, increasing the crack resistance by mode mixity [60], and reducing the crack driving force by mode mixity [32,33,72]. In section 3.2, we've shown an example estimation of how these mechanisms contribute to the toughness of the lamellar structure.

It should be noted that the above discussion focuses on the propagation of a single crack. Distributed cracking can introduce additional toughness to the material, e.g., microcracking [73,74], multiple crack initiation [61], and crack bridging [75]. Discussions about these mechanisms can be found in the corresponding references.

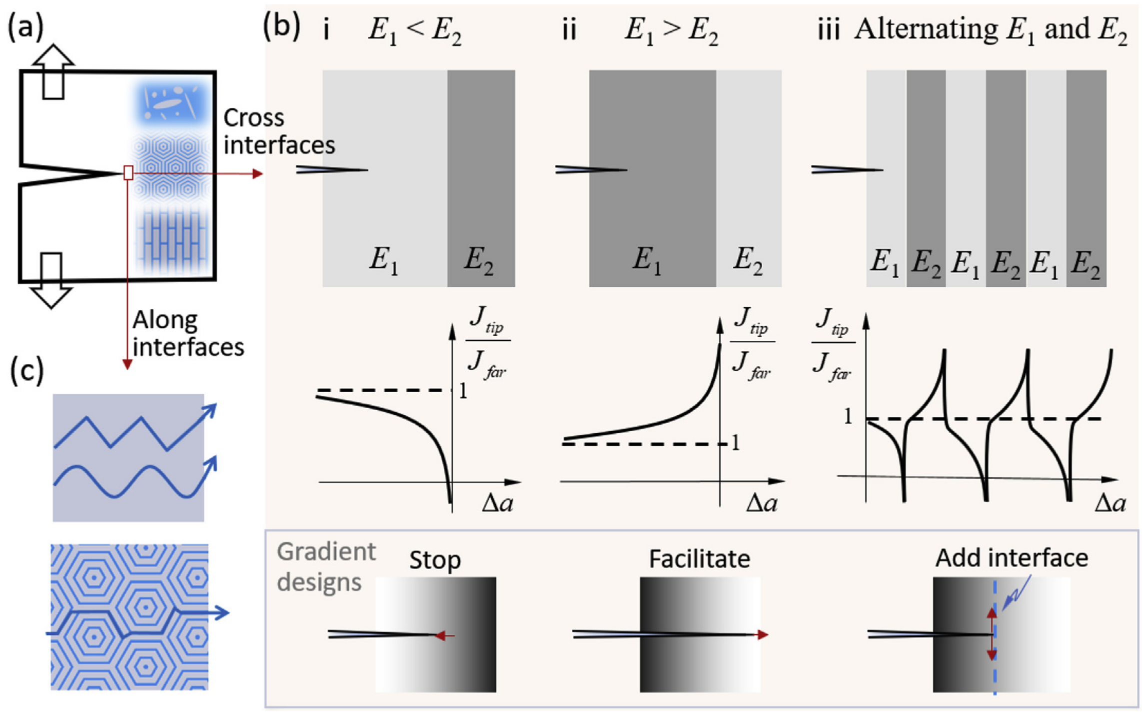

Fig. 10. Heterogeneity makes composites tougher. (a) Heterogeneous materials under CT fracture test. (b) Three typical cases of material property variations when cracks propagate across interfaces: (i) $E_1 < E_2$, (ii) $E_1 > E_2$, and (iii) alternating E_1 and E_2. The second row shows the corresponding cracking driving force near the interface, the third row depicts the theoretical implications for designing gradient materials. (c) Cracks are confined at the weak interfaces.

5. Conclusions

In summary, we have 3D printed biomimetic composites with five different bioinspired microstructures and used fracture tests to characterize their crack resistance curves. Aided by strain field visualization and theoretical analysis, the underlying toughening mechanisms were analyzed quantitatively. The rotating plywood structure exhibits the highest work of fracture and presents a “J” shaped *R*-curve due to a crack twisting mechanism. Strong and tough brick and mortar structures are achieved by synergistic work of the staggered microstructure, interfacial asperity, and hard bridges. The concentric hexagonal structure shows comparable toughness to the rotating plywood structure, and its high toughness originates from periodic cycles of crack deflection and hard phase breakage. By contrast, the lamellar structures exhibit relatively small toughness improvement. Therefore, it is recommended to use them in combination with multi-crack initiation mechanisms, like their biomaterial counterpart. It is also highlighted that a “J” shaped *R*-curve tends to have a larger critical energy release rate and tolerates a longer crack, while a “Γ” shaped *R*-curve provides better crack initiation resistance.

Moreover, guidelines for the microstructural design and criteria for obtaining favorable failure patterns were presented. Examples include the condition to obtain deflected cracks around the concentric hexagons, and how material property should be selected to controls the “J” shaped *R*-curve of the rotating plywood structure. Furthermore, the effect of heterogeneity is summarized as 1) property variations that stop crack penetration and 2) crack propagation along soft interfaces that facilitate progressive damages. Local “J” shapes are found common in the *R*-curves of heterogeneous materials, which are formed when cracks propagate from soft materials toward hard materials. These results provide useful information on the relationship between material microstructure and crack resistance, which will boost the design of stronger and tougher materials.

Competing interest

The authors declare no competing financial interests.

Acknowledgment

This work is partly supported by the National Science Foundation (CMMI-1462270). The authors thank Stephen Zakoworotny for assistance in the experiment. The authors acknowledge the use of the Center for Functional Nanomaterials facility at Brookhaven National Laboratory.

Appendix A. Supplementary data

Supplementary data to this article can be found online at https://doi.org/10.1016/j.actamat.2019.04.052.

References

[1] R.O. Ritchie, The conflicts between strength and toughness, Nat. Mater. 10 (11) (2011) 817.
[2] Z. Jia, Y. Yu, L. Wang, Learning from nature: use material architecture to break the performance tradeoffs, Mater. Des. 168 (2019) 107650.
[3] M.F. Ashby, Materials Selection in Mechanical Design, Elsevier Science & Technology Books, 2016.
[4] S.E. Naleway, M.M. Porter, J. McKittrick, M.A. Meyers, Structural design elements in biological materials: application to bioinspiration, Adv. Mater. 27 (37) (2015) 5455–5476.
[5] M.A. Meyers, J. McKittrick, P.-Y. Chen, Structural biological materials: critical mechanics-materials connections, Science 339 (6121) (2013) 773–779.

[6] W. Clegg, K. Kendall, N.M. Alford, T. Button, J. Birchall, A simple way to make tough ceramics, Nature 347 (6292) (1990) 455–457.
[7] E. Munch, M.E. Launey, D.H. Alsem, E. Saiz, A.P. Tomsia, R.O. Ritchie, Tough, bio-inspired hybrid materials, Science 322 (5907) (2008) 1516–1520.
[8] Z. Jia, T. Li, F.-p. Chiang, L. Wang, An experimental investigation of the temperature effect on the mechanics of carbon fiber reinforced polymer composites, Compos. Sci. Technol. 154 (2018) 53–63.
[9] X. Wu, M. Yang, F. Yuan, G. Wu, Y. Wei, X. Huang, Y. Zhu, Heterogeneous lamella structure unites ultrafine-grain strength with coarse-grain ductility, Proc. Natl. Acad. Sci. Unit. States Am. 112 (47) (2015) 14501–14505.
[10] P. Podsiadlo, A.K. Kaushik, E.M. Arruda, A.M. Waas, B.S. Shim, J. Xu, H. Nandivada, B.G. Pumplin, J. Lahann, A. Ramamoorthy, Ultrastrong and stiff layered polymer nanocomposites, Science 318 (5847) (2007) 80–83.
[11] Y.A. Shin, S. Yin, X. Li, S. Lee, S. Moon, J. Jeong, M. Kwon, S.J. Yoo, Y.-M. Kim, T. Zhang, Nanotwin-governed toughening mechanism in hierarchically structured biological materials, Nat. Commun. 7 (2016) 10772.
[12] L.R. Meza, A.J. Zelhofer, N. Clarke, A.J. Mateos, D.M. Kochmann, J.R. Greer, Resilient 3D hierarchical architected metamaterials, Proc. Natl. Acad. Sci. Unit. States Am. 112 (37) (2015) 11502–11507.
[13] L. Wang, J. Lau, E.L. Thomas, M.C. Boyce, Co-continuous composite materials for stiffness, strength, and energy dissipation, Adv. Mater. 23 (13) (2011) 1524–1529.
[14] J.R. Raney, B.G. Compton, J. Mueller, T.J. Ober, K. Shea, J.A. Lewis, Rotational 3D printing of damage-tolerant composites with programmable mechanics, Proc. Natl. Acad. Sci. Unit. States Am. (2018) 201715157.
[15] L.S. Dimas, G.H. Bratzel, I. Eylon, M.J. Buehler, Tough composites inspired by mineralized natural materials: computation, 3D printing, and testing, Adv. Funct. Mater. 23 (36) (2013) 4629–4638.
[16] J.H. Martin, B.D. Yahata, J.M. Hundley, J.A. Mayer, T.A. Schaedler, T.M. Pollock, 3D printing of high-strength aluminium alloys, Nature 549 (7672) (2017) 365.
[17] F. Libonati, G.X. Gu, Z. Qin, L. Vergani, M.J. Buehler, Bone-inspired materials by design: toughness amplification observed using 3D printing and testing, Adv. Eng. Mater. 18 (8) (2016) 1354–1363.
[18] L. Liu, Y. Li, Predicting the mixed-mode I/II spatial damage propagation along 3D-printed soft interfacial layer via a hyperelastic softening model, J. Mech. Phys. Solids 116 (2018) 17–32.
[19] G.X. Gu, F. Libonati, S.D. Wettermark, M.J. Buehler, Printing nature: unraveling the role of nacre's mineral bridges, J. Mech. Behav. Biomed. Mater. 76 (2017) 135–144.
[20] L. Liu, Q. Ding, Y. Zhong, J. Zou, J. Wu, Y.-L. Chiu, J. Li, Z. Zhang, Q. Yu, Z. Shen, Dislocation network in additive manufactured steel breaks strength–ductility trade-off, Mater. Today 21 (4) (2017) 354–361.
[21] J.J. Martin, B.E. Fiore, R.M. Erb, Designing bioinspired composite reinforcement architectures via 3D magnetic printing, Nat. Commun. 6 (2015) 8641.
[22] B.G. Compton, J.A. Lewis, 3D-printing of lightweight cellular composites, Adv. Mater. 26 (34) (2014) 5930–5935.
[23] Z. Jia, Y. Yu, S. Hou, L. Wang, Biomimetic architected materials with improved dynamic performance, J. Mech. Phys. Solids 125 (2019) 178–197.
[24] H. Ming-Yuan, J.W. Hutchinson, Crack deflection at an interface between dissimilar elastic materials, Int. J. Solids Struct. 25 (9) (1989) 1053–1067.
[25] P. Fratzl, H.S. Gupta, F.D. Fischer, O. Kolednik, Hindered crack propagation in materials with periodically varying Young's modulus—lessons from biological materials, Adv. Mater. 19 (18) (2007) 2657–2661.
[26] J. Toribio, V. Kharin, Role of fatigue crack closure stresses in hydrogen-assisted cracking, in: Advances in Fatigue Crack Closure Measurement and Analysis: Second Volume, ASTM International, 1999.
[27] Z. Suo, Singularities, interfaces and cracks in dissimilar anisotropic media, Proc. Roy. Soc. Lond. A 427 (1873) (1990) 331–358.
[28] Z. Suo, G. Bao, B. Fan, T. Wang, Orthotropy rescaling and implications for fracture in composites, Int. J. Solids Struct. 28 (2) (1991) 235–248.
[29] J.W. Hutchinson, Z. Suo, Mixed mode cracking in layered materials, Adv. Appl. Mech. (1991) 63–191. Elsevier.
[30] M.Y. He, A.G. Evans, J.W. Hutchinson, Crack deflection at an interface between dissimilar elastic materials: role of residual stresses, Int. J. Solids Struct. 31 (24) (1994) 3443–3455.
[31] O. Kolednik, J. Predan, F. Fischer, P. Fratzl, Improvements of strength and fracture resistance by spatial material property variations, Acta Mater. 68 (2014) 279–294.
[32] K.T. Faber, A.G. Evans, Crack deflection processes—I, Theory, Acta Metall. 31 (4) (1983) 565–576.
[33] N. Suksangpanya, N.A. Yaraghi, D. Kisailus, P. Zavattieri, Twisting cracks in Bouligand structures, J. Mech. Behav. Biomed. Mater. 76 (2017) 38–57.
[34] Y. Wei, H. Gao, A.F. Bower, Numerical simulations of crack deflection at a twist-misoriented grain boundary between two ideally brittle crystals, J. Mech. Phys. Solids 57 (11) (2009) 1865–1879.
[35] Y. Gao, Z. Guo, Z. Song, H. Yao, Spiral interface: a reinforcing mechanism for laminated composite materials learned from nature, J. Mech. Phys. Solids 109 (2017) 252–263.
[36] F. Barthelat, H. Tang, P. Zavattieri, C.-M. Li, H. Espinosa, On the mechanics of mother-of-pearl: a key feature in the material hierarchical structure, J. Mech. Phys. Solids 55 (2) (2007) 306–337.
[37] U.G. Wegst, H. Bai, E. Saiz, A.P. Tomsia, R.O. Ritchie, Bioinspired structural materials, Nat. Mater. 14 (1) (2015) 23.
[38] L. Grunenfelder, N. Suksangpanya, C. Salinas, G. Milliron, N. Yaraghi, S. Herrera, K. Evans-Lutterodt, S. Nutt, P. Zavattieri, D. Kisailus, Bio-inspired impact-resistant composites, Acta Biomater. 10 (9) (2014) 3997–4008.
[39] G.X. Gu, M. Takaffoli, M.J. Buehler, Hierarchically enhanced impact resistance of bioinspired composites, Adv. Mater. 29 (28) (2017).
[40] J.C. Weaver, G.W. Milliron, A. Miserez, K. Evans-Lutterodt, S. Herrera, I. Gallana, W.J. Mershon, B. Swanson, P. Zavattieri, E. DiMasi, The stomatopod dactyl club: a formidable damage-tolerant biological hammer, Science 336 (6086) (2012) 1275–1280.
[41] A. Bigi, M. Burghammer, R. Falconi, M.H. Koch, S. Panzavolta, C. Riekel, Twisted plywood pattern of collagen fibrils in teleost scales: an X-ray diffraction investigation, J. Struct. Biol. 136 (2) (2001) 137–143.
[42] T. Yamamoto, T. Domon, S. Takahashi, N. Islam, R. Suzuki, Twisted plywood structure of an alternating lamellar pattern in cellular cementum of human teeth, Anat. Embryol. 202 (1) (2000) 25–30.
[43] Z. Zhang, Y.-W. Zhang, H. Gao, On optimal hierarchy of load-bearing biological materials, Proc. R. Soc. Lond. B Biol. Sci. 278 (1705) (2011) 519–525.
[44] J. Kruzic, S. Kuskowski, R. Ritchie, Simple and accurate fracture toughness testing methods for pyrolytic carbon/graphite composites used in heart-valve prostheses, J. Biomed. Mater. Res. A 74 (3) (2005) 461–464.
[45] Y. Chen, T. Li, Z. Jia, F. Scarpa, C.-W. Yao, L. Wang, 3D printed hierarchical honeycombs with shape integrity under large compressive deformations, Mater. Des. 137 (2018) 226–234.
[46] H. Yao, Z. Song, Z. Xu, H. Gao, Cracks fail to intensify stress in nacreous composites, Compos. Sci. Technol. 81 (2013) 24–29.
[47] F. Song, A. Soh, Y. Bai, Structural and mechanical properties of the organic matrix layers of nacre, Biomaterials 24 (20) (2003) 3623–3631.
[48] M.R. O'Masta, L. Dong, L. St-Pierre, H. Wadley, V.S. Deshpande, The fracture toughness of octet-truss lattices, J. Mech. Phys. Solids 98 (2017) 271–289.
[49] T. Li, Y. Chen, L. Wang, Enhanced fracture toughness in architected interpenetrating phase composites by 3D printing, Compos. Sci. Technol. 167 (2018) 251–259.
[50] F. Barthelat, H. Espinosa, An experimental investigation of deformation and fracture of nacre–mother of pearl, Exp. Mech. 47 (3) (2007) 311–324.
[51] G.C. Sih, P. Paris, G.R. Irwin, On cracks in rectilinearly anisotropic bodies, Int. J. Fract. Mech. 1 (3) (1965) 189–203.
[52] S. Fan, B. Yilong, Mineral bridges of nacre and its effects, Acta Mech. Sin. 17 (3) (2001) 251.
[53] R. Wang, Z. Suo, A. Evans, N. Yao, I. Aksay, Deformation mechanisms in nacre, J. Mater. Res. 16 (9) (2001) 2485–2493.
[54] S. Askarinejad, N. Rahbar, Toughening mechanisms in bioinspired multilayered materials, J. R. Soc. Interface 12 (102) (2015) 20140855.
[55] H.-M. Yang, Y.-C. Chan, T.-H. Hsu, H.-W. Chen, J.-W. Lee, J.-G. Duh, P.-Y. Chen, Synthesis and characterization of nacre-inspired zirconia/polyimide multilayer coatings by a hybrid sputtering and pulsed laser deposition technique, Surf. Coating. Technol. 284 (2015) 118–128.
[56] M.R. Begley, N.R. Philips, B.G. Compton, D.V. Wilbrink, R.O. Ritchie, M. Utz, Micromechanical models to guide the development of synthetic 'brick and mortar'composites, J. Mech. Phys. Solids 60 (8) (2012) 1545–1560.
[57] F. Barthelat, A.K. Dastjerdi, R. Rabiei, An improved failure criterion for biological and engineered staggered composites, J. R. Soc. Interface 10 (79) (2013) 20120849.
[58] H. Gao, Application of fracture mechanics concepts to hierarchical biomechanics of bone and bone-like materials, Int. J. Fract. 138 (1–4) (2006) 101.
[59] Z. Xie, H. Yao, Crack deflection and flaw tolerance in" brick-and-mortar" structured composites, International Journal of Applied Mechanics 6 (02) (2014) 1450017.
[60] A.G. Evans, J.W. Hutchinson, Effects of non-planarity on the mixed mode fracture resistance of bimaterial interfaces, Acta Metall. 37 (3) (1989) 909–916.
[61] S. Kamat, H. Kessler, R. Ballarini, M. Nassirou, A.H. Heuer, Fracture mechanisms of the Strombus gigas conch shell: II-micromechanics analyses of multiple cracking and large-scale crack bridging, Acta Mater. 52 (8) (2004) 2395–2406.
[62] S. Kamat, X. Su, R. Ballarini, A. Heuer, Structural basis for the fracture toughness of the shell of the conch Strombus gigas, Nature 405 (6790) (2000) 1036.
[63] G.X. Gu, M. Takaffoli, M.J. Buehler, Hierarchically enhanced impact resistance of bioinspired composites, Adv. Mater. 29 (28) (2017) 1700060.
[64] L. Kuhn-Spearing, H. Kessler, E. Chateau, R. Ballarini, A. Heuer, S. Spearing, Fracture mechanisms of the Strombus gigas conch shell: implications for the design of brittle laminates, J. Mater. Sci. 31 (24) (1996) 6583–6594.
[65] J. Chang, J.-q. Xu, Y. Mutoh, A general mixed-mode brittle fracture criterion for cracked materials, Eng. Fract. Mech. 73 (9) (2006) 1249–1263.
[66] Z.P. Bazant, J. Planas, Fracture and Size Effect in Concrete and Other Quasibrittle Materials, CRC press, 1997.
[67] F. Fischer, O. Kolednik, J. Predan, H. Razi, P. Fratzl, Crack driving force in twisted plywood structures, Acta Biomater. 55 (2017) 349–359.
[68] D. Bajaj, D.D. Arola, On the R-curve behavior of human tooth enamel, Biomaterials 30 (23–24) (2009) 4037–4046.
[69] T.L. Anderson, Fracture Mechanics: Fundamentals and Applications, CRC press, 2017.
[70] Z. Liu, Z. Weng, Z.-F. Zhai, N. Huang, Z.-J. Zhang, J. Tan, C. Jiang, D. Jiao, G. Tan,

J. Zhang, Hydration-induced nano-to micro-scale self-recovery of the tooth enamel of the giant panda, Acta Biomater. 81 (2018) 267–277.
[71] N. Simha, F. Fischer, O. Kolednik, C. Chen, Inhomogeneity effects on the crack driving force in elastic and elastic–plastic materials, J. Mech. Phys. Solids 51 (1) (2003) 209–240.
[72] X. Zeng, Y. Wei, Crack deflection in brittle media with heterogeneous interfaces and its application in shale fracking, J. Mech. Phys. Solids 101 (2017) 235–249.
[73] A. Evans, K. Faber, Crack-growth resistance of microcracking brittle materials, J. Am. Ceram. Soc. 67 (4) (1984) 255–260.
[74] J.W. Hutchinson, Crack tip shielding by micro-cracking in brittle solids, Acta Metall. 35 (7) (1987) 1605–1619.
[75] B. Budiansky, J.C. Amazigo, A.G. Evans, Small-scale crack bridging and the fracture toughness of particulate-reinforced ceramics, J. Mech. Phys. Solids 36 (2) (1988) 167–187.